3D reduced graphene oxide scaffolds with a combinatorial fibrous-porous architecture for neural tissue engineering

André F. Girão[1,2], Joana Sousa[1], Ana Domínguez-Bajo[2], Ankor González-Mayorga[3], Igor Bdikin[1], Eulalia Pujades-Otero[4], Nieves Casañ-Pastor[4], María Jesús Hortigüela[1], Gonzalo Otero-Irurueta[1], António Completo[1], María Concepción Serrano[2] and Paula A.A.P. Marques[1*]*

[1] TEMA, Department of Mechanical Engineering, University of Aveiro (UA), Aveiro, 3810-193, Portugal

[2] Instituto de Ciencia de Materiales de Madrid (ICMM), Consejo Superior de Investigaciones Científicas (CSIC), Calle Sor Juana Inés de la Cruz 3, Madrid, 28049, Spain

[3] Laboratory of Interfaces for Neural Repair, Hospital Nacional de Parapléjicos, SESCAM, Finca la Peraleda s/n, Toledo, 45071, Spain

[4] Instituto de Ciencia de Materiales de Barcelona (ICMAB), Consejo Superior de Investigaciones Científicas (CSIC), Campus de la Universidad Autónoma de Barcelona, 08193, Barcelona, Spain

KEYWORDS: Reduced graphene oxide, 3D scaffold, fibrous-porous architecture, electrospinning, neural tissue engineering

ABSTRACT

Graphene oxide (GO) assists a diverse set of promising routes to build bioactive neural microenvironments by easily interacting with other biomaterials to enhance their bulk features or, alternatively, self-assembling towards the construction of biocompatible systems with specific 3D geometries. Herein, we firstly modulate both size and available oxygen groups in GO nanosheets in order to adjust the physicochemical and biological properties of polycaprolactone-gelatin electrospun nanofibrous systems. Results show that the incorporation of customized GO nanosheets modulates the properties of the nanofibres and, subsequently, markedly influence the viability of neural progenitor cell cultures. Interestingly, the partially reduced GO (rGO) nanosheets with larger dimensions trigger the best cell response, while the rGO nanosheets with smaller size provoke an accentuated decrease in the cytocompatibility of the resulting electrospun meshes. Then, the most auspicious nanofibres are synergistically accommodated onto the surface of 3D rGO heterogeneous porous networks, giving rise to fibrous-porous combinatorial architectures suitable for enhancing adhesion and differentiation of neural cells. By varying the chemical composition of the nanofibres, it is possible to adapt their performance as physical crosslinkers for the rGO sheets, leading to the modulation of both pore size and structural/mechanical integrity of the scaffold. Importantly, the biocompatibility of the resultant fibrous-porous systems is not compromised after 14 days of cell culture, including standard differentiation patterns of neural progenitor cells. Overall, in the light of these *in vitro* results, the reported scaffolding approach presents not only an indisputable capacity to support highly viable and interconnected neural circuits, but also the potential to unlock novel strategies for neural tissue engineering applications.

1. INTRODUCTION

During the last years, graphene-based materials have consistently emerged as crucial building blocks for developing advanced biomedical platforms proficient to integrate the next generation of neural regenerative therapies.[1-3] Particularly, the manipulation of the oxygen moieties located onto the graphene oxide (GO) surface is currently boosting the fabrication of a wide range of tissue engineering (TE) scaffolds able to trigger and regulate specific differentiation patterns of neural stem cells (NSCs).[4] The structural arrangement of GO nanosheets present not only sp^2 hybridized carbon atoms similar to the monolayer of pristine graphene, but also a distribution of sp^3 regions where the carbons are linked with epoxy and hydroxyl functionalities onto the basal plane, and with carbonyl and carboxyl groups onto the plane edges.[5] It is the reactivity of these hydrophilic zones, together with the morphological characteristics (e.g. lateral size) of the nanosheets, that define the capacity of GO to directly interfere with molecular mechanisms responsible for modulating the behavior of neurons[6] and astrocytes.[7] Both *in vitro*[8] and *in vivo*[9] studies have recently reported that the cellular internalization of small GO flakes favored the ability of neurons to preferentially boost inhibitory synapses across neuronal networks rather than excitatory neurotransmissions. Complementarily, alternative strategies to adjust neural cell responses such as adhesion, differentiation and neurite sprouting/outgrowth rely on anchoring bioactive functionalities onto the oxygen species of GO with the final purpose of developing biocompatible substrates with particular surface charge and chemistry.[10-12] For example, GO coatings promoted fibronectin attachment onto a hierarchical patterned substrate, improving the focal adhesion and neuronal differentiation of human NSCs.[13] This enhanced ability of GO to establish interactions with biomolecules, cells and polymers can be further modulated by chemical and thermal processes suitable to diminish its oxidative state towards the production of

reduced graphene oxide (rGO).[14] As the increase of the C/O ratio augments the electrical conductivity and the hydrophobicity of the rGO nanosheets, it tailors cell-material interactions responsible for modulating biological processes such as inflammatory responses *in vivo*[15] and predominant differentiation of NSCs into viable neurons rather than glia.[16]

Based on this tunability, both GO and rGO are effectively upgrading the biochemical and biophysical gradients essential to shape 3D neural microenvironments such as nanofibrous and porous systems. The integration of these nanomaterials in the composition of electrospun nanofibres proved to be a feasible and versatile approach to complement biomimetic topographic cues with optimal biological, electrical and/or mechanical features.[17-18] For example, surface properties of nanofibres (e.g. chemistry, roughness, wettability) composed of polycaprolactone (PCL)[19] and poly-L-lactide[20] can be efficiently adjusted by GO coatings for enhancing NSCs differentiation into oligodendrocytes and proliferation of Schwann cells, respectively. A more progressive strategy was described by Wang et al.,[21] who efficaciously modulated the functionality of cultured neural progenitor cells (NPCs) by controlling the release of methylene blue from the surface of a GO-coated poly(lactic-co-glycolic acid) electrospun scaffold for Alzheimer's disease therapeutics. Specifically, NPCs cultured on the scaffolds remained quiescent due to the activation of autophagy signaling pathways by methylene blue, diminishing tau phosphorylation and then protecting these cells from apoptosis. Importantly, with the purpose of influencing cell responses, electrospinning polymer/graphene composite solutions could benefit from a homogeneous distribution of graphene nanosheets within the polymer matrix, thus resulting in nanofibrous networks with superior overall electrical and mechanical properties.[22] Alternatively, aligned nanofibres can be placed on top of highly conductive graphene-based substrates in order to guide neurite sprouting and outgrowth towards the formation of highly

viable neural networks *in vitro*.[23] Complementary to nanofibrous systems, recent reports have pointed out that the establishment of interconnected neural circuits could be facilitated by the capacity of graphene-based porous architectures to either deliver electrical stimuli or mimic *in vivo* conditions.[24-25] For instance, after poly-D-lysine functionalization, 3D rGO porous scaffolds induced adhesion and differentiation of embryonic neural progenitor cells (ENPCs) into both neurons (preferentially) and glia, supporting the outgrowth of dendrites and axons and the formation of synaptic connections through the pores.[26] These noteworthy results *in vitro* motivated the investigation of these rGO scaffolds in the injured rat spinal cord, where the rGO porous network promoted an enhanced infiltration of cells and extracellular matrix (ECM) components (e.g. collagen) as well as the presence of neuronal axons near to newly formed functional blood vessels.[27]

In this work, we demonstrated how the reorganization of biocompatible nanofibrous systems onto the surface of 3D rGO porous networks can remarkably support the formation of interconnected neuronal circuits *in vitro*. The validation of this original scaffolding approach was initiated with the evaluation of the effects of incorporating GO nanosheets with different sizes and C/O ratios into PCL-gelatin nanofibres. Both GO nanofillers and electrospun meshes were thoroughly characterized. In order to select the best components to integrate the final 3D combinatorial architecture, ENPCs were seeded onto the composite nanofibres and their viability assessed. Then, the best nanofibrous compositions were tested as physical crosslinkers of the rGO sheets, resulting in unique 3D fibrous-porous systems with tunable structural properties that were again challenged with ENPC cultures *in vitro* for 14 days.

2. Experimental section

2.1. Modification of GO nanosheets

The initial GO nanosheets (GO dispersion in distilled water at 4 mg/mL; Graphenea, S. A., Spain) were subjected to an ultrasonication process previously described by our group with the purpose of fabricating nano-GO (GO_n) flakes.[28] Briefly, the GO dispersion was continuously stirred while sonicated by a 750 W ultrasonic processor (Amplitude = 20%; Bioblock Scientific VibraCell, France) equipped with a 20 mm probe. The ultrasonication time was up to 90 min in total, during which the active periods (1 min) were intercalated by pause periods of 1 min to avoid overheating. The resulting GO_n dispersion was centrifuged to remove remaining original GO sheets. Furthermore, the GO and GO_n nanosheets were chemically reduced to rGO and rGO_n, respectively, by adding a diluted hydrazine hydrate solution (dilution factor: 1.5; $N_2H_4 \cdot H_2O$, 50-60%, Sigma-Aldrich) into the GO and GO_n dispersions at room temperature (RT) for 24 h (1 μL of $N_2H4 \cdot H_2O$ for 4 mg of nanomaterial).

2.2. Characterization of the nanomaterials

The particle size of the GO_n sheets was measured after 30, 60 and 90 min of ultrasonication by using dynamic light scattering analyses (DLS; Zetasizer Nano ZS90, Malvern Instruments, UK) at RT and pH of approximately 4. The topography of the GO, GO_n, rGO and rGO_n flakes was accessed by atomic force microscopy (AFM) measurements (Veeco AFM Multimode Nanoscope (IV) MMAFM-2, USA, with conductive Si cantilevers from Nanosensors with a nominal force constant 15 N/m probe). Previously to the chemical analysis of their surface, the GO, GO_n, rGO and rGO_n water dispersions were freeze-dried at -80 °C (Teslar lyoQuest HT-40, Beijer Electronics Products AB, Sweden). Then, X-ray photoelectron spectroscopy (XPS) spectra were

acquired in an ultra-high vacuum system with a base pressure of $2x10^{-10}$ mbar. They were recorded at normal emission take-off angle and with a pass-energy of 20 eV, which provides an overall instrumental peak broadening of about 0.5 eV. This system is equipped with a hemispherical electron energy analyzer (SPECS Phoibos 150), a delay-line detector and a monochromatic AlKα (1486.74 eV) X-ray source. The structural characterization and interlayer spacing of the nanomaterials were determined by X-ray diffraction (XRD; Rigaku SmartLab diffractometer, Rigaku corporation, Japan) using Cu Kα radiation (λ = 1.5406 Å) and operated at 40 kV and 30 mA. The XRD patterns were collected within the range of 5 º < 2θ < 80 º with a scan speed of 1 º/min. Raman spectra of the nanomaterials (FT Raman Bruker RFS 100/S, Brucker Corporation, USA) were acquired by using a Nd:YAG laser with excitation at 1064 nm.

2.3. Fabrication of electrospun nanofibres

PCL (80 kDa; Sigma-Aldrich) and gelatin (porcine skin; Sigma Aldrich) were dissolved in 2,2,2-trifluoroethanol (TFE; Tokyo Chemical Industry, Japan) with concentration of 10% w/v. After 12 h under mechanical stirring, both solutions were mixed (1:1, v:v) and 0.2% (v:v) of acetic acid (Sigma Aldrich) was added in order to homogenize the final PCL-gelatin solution. This solution was electrospun (NANON-01A, MECC Co. Ltd., Japan) at a controlled flow rate (1 mL/h) through a 21-gauge blunt-tip needle with applied voltage of 20 kV. A rotating drum (width = 6 cm; diameter = 10 cm; velocity = 1500 RPM) was used as a collector at a working distance of 15 cm. The final PCL-gelatin electrospun system presented a thickness of approximately 100 μm and it was named PG. For fabricating PG-GO, PG-GO_n, PG-rGO and PG-rGO_n nanofibrous networks, the corresponding nanomaterial was firstly dispersed in TFE and then mixed with the PCL-gelatin solution under continuous stirring for 30 min. The final homogenized electrospun solutions were prepared at a concentration of 10% w/v

(nanomaterial:polymer, w:w, ratio of 0.6%) and were electrospun using similar parameters as the PCL-gelatin solution.

2.4. Characterization of electrospun nanofibres

The structural properties of all electrospun systems were characterized by Raman and XRD analyses. To study the morphology of the nanofibres, including their diameter, ImageJ software (free software from National Institutes of Health by Wayne Rasband) was used to analyze images (n = 10 per material) acquired by scanning electron microscopy (SEM; Hitachi SU 70, Hitachi High-Technologies Corporation, Japan). For mechanical testing, the electrospun nanofibres were sectioned into rectangles (width = 5 mm; length = 15 mm; thickness of approximately 100 μm measured with a micrometer) and stretched until 150% of strain at a rate of 1 mm/min (Shimadzu MMT-101N, Shimadzu Scientific Instruments, Japan). After a pre-charge of 0.07 N, the tensile moduli and elongations at break of the samples ($n \geq 5$ per material) were calculated from stress-strain curves. Electrochemical impedance spectroscopy (EIS) measurements, using a potentiostat/ galvanostat (Bio-logic Science Instruments, model VSP), were performed on samples immersed in phosphate buffered solution (PBS; in mM: 38.7 NaH_2PO_4, 61.3 Na_2HPO_4, pH 7.4) at RT with the same electrode geometrical area (cylinder with diameter = 3 mm and high = 2 mm). After 1 h of incubation in the electrolyte solution, it was used a three-electrode electrochemical cell to perform the measurements: the working electrode was the nanofibrous system under study; the counter electrode was a Pt foil (rectangular shape with area = 1.5 cm^2) and the pseudoreference electrode was a Pt wire (diameter = 0.5 mm). A Pt sheet (area = 0.1 cm^2) and a Glassy Carbon electrode (G.C.; area = 0.07 cm^2; Bio-logic Science Instruments) were also used as working electrodes for comparison purposes. A sinusoidal AC

wave of 10 mV amplitude was used at open circuit potential (vs Pt = vs Ag/AgCl) and measurements made in the 100 mHz – 100 kHz frequency range.

2.5. Fabrication of 3D fibrous-porous scaffolds

The PG and PG-rGO electrospun meshes were firstly cut into small pieces (width = 5 mm; length = 5 mm) and dispersed in distilled water. The nanofibres were further fragmented into tiny pieces by using a high-speed blender for 30 min at RT. The obtained PG and PG-rGO dispersions were mixed with a rGO aqueous solution, leading to blends of 6 mg/mL (ratio of 1:1, w:w) that formed hydrogel-like structures. These hydrogels were placed into cylindrical Teflon moulds (diameter = 5 mm; height = 5 mm) and kept at -20 °C overnight. Then, after a lyophilization process at -80 °C, the fibrous-porous PG+rGO and PG-rGO+rGO constructions (diameter = between 3 and 4 mm; height ~ 5 mm) were obtained and named after "3D-PG scaffold" and "3D-rGO scaffold", respectively.

2.6. Characterization of 3D fibrous-porous scaffolds

Attenuated total reflectance Fourier transform infrared spectra (ATR-FTIR; Bruker Tensor 27 FT-IR spectrometer, Brucker Corporation, USA) of the scaffolds and their components were recorded between 4000 and 350 cm^{-1}, with a resolution of 4 cm^{-1} and 256 scans. The topography of the scaffolds, including pore size, was estimated from SEM images (n = 10 per scaffold; Hitachi TM 4000 plus, Hitachi High-Technologies Corporation, Japan) by using ImageJ software. For evaluating the water uptake capacity of both 3D-PG and 3D-rGO scaffolds, the samples (n = 5 per scaffold) were immersed into distilled water for 48 h at room temperature in order to determine their swelling ratios for several time points (1, 3, 6, 24 and 48 h) with the following formula:

$$R = \frac{(W_s - W_d)}{W_d}$$

where R is the swelling ratio (mg/mg), W_s is the weight of the swollen scaffold and W_d is the weight of the dried scaffold. The mechanical properties of the swollen 3D-PG and 3D-rGO scaffolds were studied by compressing the specimens ($n \geq 5$ per scaffold) at a rate of 1 mm/min after a pre-charge of 0.07 N with the purpose of calculating their compressive moduli from the linear regime of the respective stress-strain curves.

2.7. Isolation and culture of rat ENPCs

Prior to cell culture, the electrospun nanofibres and 3D scaffolds were sterilized under UV radiation for 30 min and then thoroughly washed with sterile water. The substrates were then immersed into a poly-L-lysine (PLL) aqueous solution (45 μg/mL) for 12 h at RT before being washed twice with sterile water and finally conditioned for 2-3 h (at 37 °C under a 5% CO_2 atmosphere) in culture medium (Neurobasal™ media containing 2% of B-27 supplement, 100 UI/mL of streptomycin, 100 UI/mL of penicillin and 1 mM of L-glutamine). ENPCs were extracted from cerebral cortices of E18 Wistar rat embryos as previously described.[29-30] Cell density for seeding was selected to assure colonization of substrates, being 75 x 10^3 and 150 x 10^3 cells for electrospun nanofibres and 3D scaffolds, correspondingly. Cells were contained into a small amount of media (500 μL for electrospun nanofibres and ~10 μL for 3D scaffolds) deposited on the materials surface and allowed to attach for 10 min, after which the substrates were totally covered with complete cell culture media and then incubated for up to 14 days. Cell media was half replaced every 4 days. PLL-coated glass coverslips under similar culture conditions to electrospun scaffolds were used as a control.

2.8. Cell morphology studies

After 14 days of culture, the morphological features of the cells were analysed by SEM (Hitachi S-3000N and Hitachi TM 4000 plus, Hitachi High-Technologies Corporation, Japan). Cultured samples were rinsed with PBS and then fixed with glutaraldehyde (2.5% in PBS; Sigma-Aldrich) for 45 min at RT. After this period, the samples were washed in distilled water and a standard dehydration protocol took place as the water was gradually replaced using a sequential series of ethanol solutions (2 washes of 15 min each) and a final dehydration in absolute ethanol for 30 min. The samples were left to dry at RT before being mounted in stubs and coated with gold under vacuum conditions.

2.9. Cell viability studies

Cell viability was measured at 14 days of culture by using a Live/Dead® viability kit according to the manufacturer's instructions (Thermo-Fisher). Briefly, the live and dead cells were stained by calcein and ethidium homodimer-1 (EthD-1), respectively. For evaluating the samples by confocal laser scanning microscopy (CLSM, Leica SP5, Leica microsystems, Germany), an argon laser was used to excite the fluorescence of both probes, which were then separated by using a triple dichroic filter (488/561/633). The calcein was measured at 505-570 nm (green fluorescence) and the EthD-1 was measured at 630-750 nm (red fluorescence). As previously described,[26] the collected images ($n \geq 3$ per scaffold) were analyzed using Fiji software with the aim of quantifying the areas positively stained for each particular marker with respect to the total image area.

2.10. Cell differentiation studies

A specific immune-labeling procedure was used to investigate ENPCs differentiation after 14 days of culture on the different substrates. Briefly, cells were fixed with paraformaldehyde (4% in PBS, Sigma-Aldrich) for 10 min at RT, rinsed with PBS and then permeabilized with saponin (0.25 in PBS + 10% of fetal bovine serum; Sigma-Aldrich) for 10 min. Map-2 and vimentin (Life technologies, USA) were selected as primary antibodies for labeling neuron and glial phenotypes, respectively. Alexa Fluor® 488 goat α-mouse IgG (H + L) and Alexa Fluor® 594 goat α-rabbit IgG (H + L) (Life technologies, USA) were the selected secondary antibodies. Primary and secondary antibodies were dissolved in PBS containing saponin (0.25%) for assuring cell permeability and fetal goat serum (2%) with the purpose of blocking non-specific binding. All incubations were carried out for 1 h in darkness at RT. In all cases, cell nuclei were labeled with DAPI (3 μM; Life technologies, USA) for 5 min. The fluorescence images were collected from the CLSM as follows: Alexa Fluor® 488 excitation at 488 nm with an argon laser and detection at 507–576 nm, Alexa Fluor® 594 at 594 nm with a helium–neon laser and detection at 625–689 nm and DAPI excitation at 405 nm with a diode UV laser and detection at 423–476 nm. From CLSM images ($n \geq 3$ per scaffold), the area positively stained for each particular marker was calculated with respect to the total substrate area in each case.

2.11. Statistical analysis

Data are expressed as mean ± standard deviation. Statistically significant differences were determined by using one-way analysis of variance (ANOVA) followed by a Scheffé test for post hoc evaluations between groups (Origin Software, $^{*}p < 0.05$; $^{**}p < 0.01$ and $^{***}p < 0.005$).

3. Results and discussion

The methodology for preparing the 3D fibrous-porous scaffolds is illustrated in Scheme 1. In brief, the physicochemical properties of GO nanosheets (commercial aqueous solution) were modified to prepare GO_n, rGO and rGO_n (1). After characterization, these nanomaterials were incorporated into the polymer matrix of PG nanofibres, resulting in electrospun systems with specific features (2). The PG and PG-rGO nanofibrous networks were then selected and fragmented before being mixed with rGO sheets to form PG+rGO and PG-rGO+rGO hydrogel-like structures. Such hydrogels were then freeze-dried, leading to final 3D fibrous-porous architectures named 3D-PG and 3D-rGO, respectively (3).

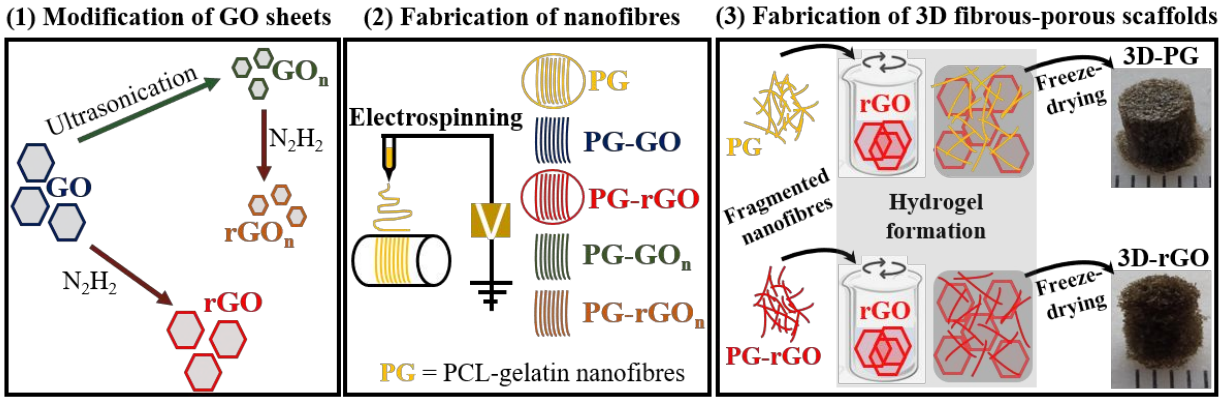

Scheme 1. Schematic illustration of fabricating the 3D porous-fibrous scaffolds.

3.1. Ultrasonication and hydrazine reduction modulates the physicochemical properties of GO nanosheets on demand

As expected, the sequential breakage of GO triggered by the ultrasonication treatment was able to successfully generate nanosheets with smaller dimensions. In detail, the DLS analysis monitored a variation of the initial average size of GO from ~ 790 nm down to ~ 250 nm after 30

min, ~ 100 nm after 60 min and, finally, to ~ 65 nm after 90 min of processing (Figure 1a). Together with this time dependent size decrease, it was also possible to observe a more homogeneous GO_n size distribution comparatively to original GO (Figure 1b). Understandably, the mechanical stirring during ultrasonication and the further removal of bigger flakes by centrifugation were valuable contributions to uniformize the dimensions of GO_n nanosheets at the end of the treatment. AFM was then used to evaluate the morphological features of GO and GO_n (Figure 1c and 1d), confirming a typical sheet-like topography for both samples as well as the presence of monolayers with thickness of 0.97 nm (Figure S1) and few-layered nanosheets. Moreover, the breakdown process of GO had a significant impact on the chemical composition of the final GO_n since the applied ultrasounds were proficient to induce temperature and pressure variations suitable for activating a hot spot atomic reduction mechanism.[28, 31] Accordingly, XPS analysis (Table 1 and Figure S2) pointed out that the increase of the C/O ratio from 2.5 (GO) to 2.8 (GO_n) was intimately related to the rupture of the C-OH and O-C-O functional groups occurring during the first stage of ultrasonication, followed by further removal of oxygen moieties (COOH and C=O) from the periphery of the nanosheets.

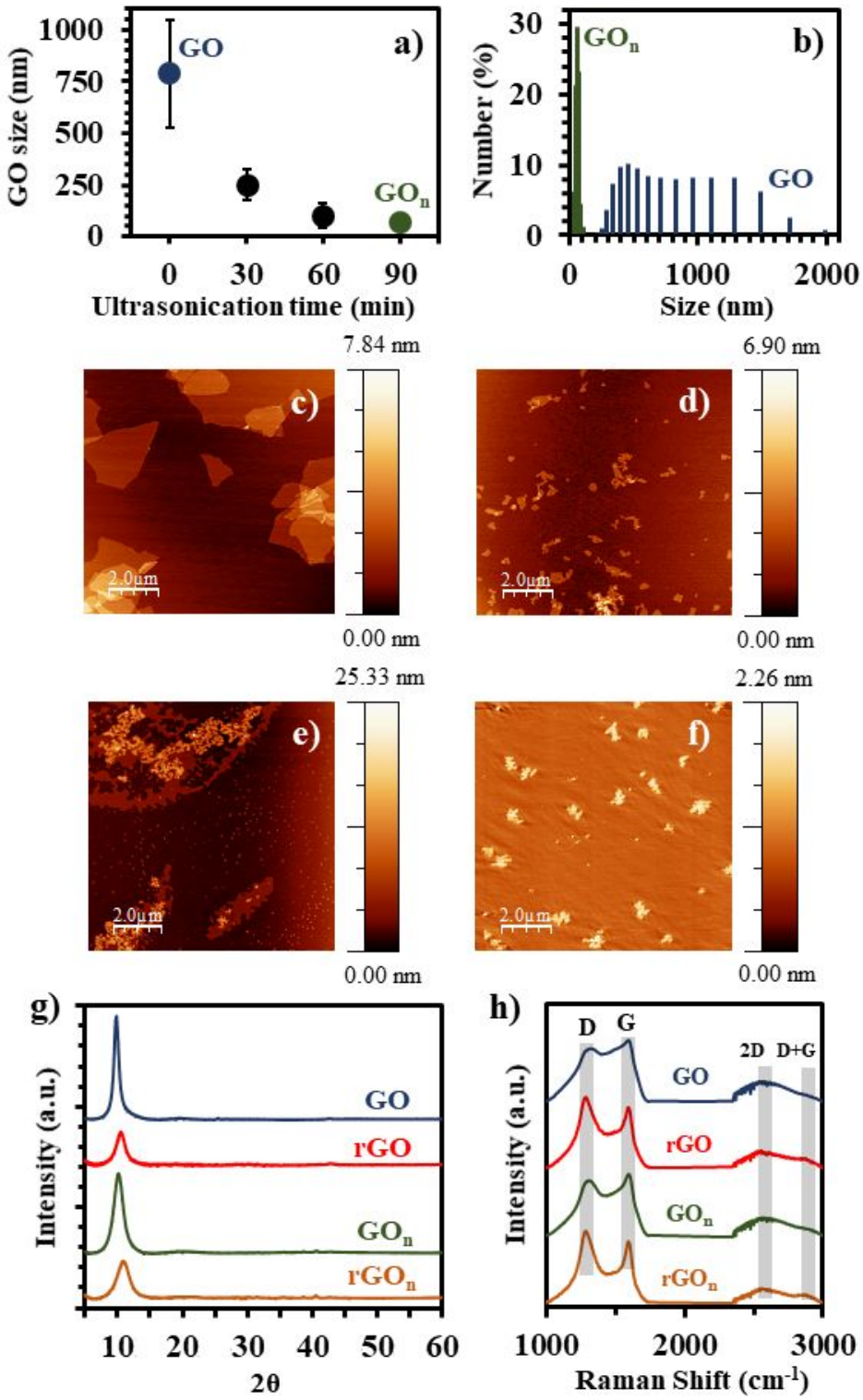

Figure 1. Characterization of GO-based nanomaterials. **a)** Variation of GO size with ultrasonication time; **b)** Size distribution of GO and GO_n nanosheets. AFM topographical view

of the nanosheets: **c)** GO; **d)** GO_n, **e)** rGO and **f)** rGO_n. **g)** XRD spectra of GO-based nanomaterials; **h)** Raman spectra of GO-based nanomaterials.

Table 1. Elemental composition of the GO-based nanomaterials obtained by XPS

Nanomaterial	Functional groups				C/O ratio
	284.5 eV	286.5 eV	288.4 eV	289.4 eV	
	C-C / C=C	C-O	C=O	O-C=O	
GO	40.2 %	45.4 %	10.4 %	4.0 %	2.5
GO_n	47.7 %	44.0 %	6.5 %	1.8 %	2.8
rGO	52.8 %	40.5 %	4.7 %	2.0 %	2.9
rGO_n	51.4 %	41.8 %	5.0 %	1.8 %	3.0

Table 1 also summarizes the effects of the hydrazine reduction on the chemistry of GO and GO_n, showing a decrease of the oxygen content from the surfaces of these nanosheets without inducing a massive reduction of their C/O ratios. The epoxy and hydroxyl groups continued to be the major oxygen components after reduction, while the carbonyl and carboxyl functionalities were removed more efficiently from the GO than from the less oxygenated GO_n nanosheets. However, the chemical compositions of the rGO (C/O ratio = 2.9) and rGO_n (C/O ratio = 3.0) were quite similar, indicating analogous oxygen residual groups after reduction independently of the nanosheets dimensions and, subsequently, a counterbalanced formation of new C-H and C=C bonds. These results are in agreement with the reduction parameters used (diluted hydrazine at RT conditions).[32-34] Based on this, theoretically, both rGO and rGO_n presented enough residual oxygen functionalities for enabling water dispersibility and feasible non-covalent bonds with polymers and biomolecules (e.g. electrostatic interactions, hydrogen bonding). According to DLS measurements, there was a noteworthy increase of rGO (~ 2.1 μm) and rGO_n (~ 400 nm) dimensions relatively to their oxygenated counterparts due to agglomeration of reduced nanosheets. This phenomenon was predominantly motivated by hydrophobic interactions and hydrogen bonds established during the hydrazine reduction

process.[35-36] In particular, during AFM analysis (Figures 1e and 1f), the heterogeneous size distribution of rGO (Figure S3) made possible to clearly observe the accumulation of smaller nanosheets on top of bigger flakes.

The structural configuration of the samples was evaluated by XRD, revealing variations as the C/O ratio and nanosheets size changed. As observed in Figure 1g, all XRD spectra presented a major diffraction peak related to the presence of oxygen functional groups onto the surface of the nanosheets and water molecules trapped between layers.[36-37] During the hydrazine reduction process of GO to rGO, there was a noticeable decrease in the intensity of this peak together with a shifting from $2\theta = 9.8$ (lattice spacing of 0.9 nm) to $2\theta = 10.5$ (lattice spacing of 0.84 nm). In agreement with XPS analysis, these events can be associated with a more accentuated elimination of oxygen moieties located near to the edges of the GO nanosheets (e.g. carboxyl).[31, 38] Indeed, as described by Park et al.,[39] the effects of hydrazine reduction progress from the edges to the basal plane of GO, leading to the establishment of π-π interactions between sheets. Consequently, as the interlayer distance narrows, the penetration of the reducing agent decreases and its efficiency on removing the oxygen groups situated on the basal plane (epoxy and hydroxyl) also drops. A parallel scenario occurred when the GO_n ($2\theta = 10.1$; lattice spacing of 0.87 nm) was chemically reduced to rGO_n ($2\theta = 10.9$; lattice spacing of 0.81 nm), confirming that, independently of nanosheets dimensions, the increasing of C/O ratio resulted on a decrease of both crystalline sizes and interlayer distance. It is also important to mention that the augment of the number of sp^2 regions during the conversion of GO into GO_n resulted on a moderate diminution of the major diffraction peak intensity and on its shifting to higher 2θ values. Raman analysis provided additional information to the structural characterization of the nanosheets. Predictably, Raman spectra (Figure 1h) enabled the recognition of the standard bands of GO,

being the D band associated to the presence of defects, while the G band is related to the crystallinity of the lattice (bond stretching of sp^2 atoms).[40] Although, theoretically, the $I_{(D)}/I_{(G)}$ ratio should decrease after reduction due to the formation of sp^2 domains, the values calculated for both rGO (1.17) and rGO_n (1.18) were higher comparatively to the GO (0.87) and GO_n (0.89). Such evolution of the $I_{(D)}/I_{(G)}$ ratios can be explained by the small spatial dimensions of the new sp^2 regions and the higher number of structural defects that remained and/or emerged within the carbon lattice as a consequence of the aggressive elimination of the oxygen functionalities.[5, 35, 41]

3.2. rGO nanosheets more favorably integrate PG electrospun nanofibres

The selected electrospinning parameters enabled the fabrication of an interconnected and uniform PG nanofibrous network, which was composed by preferentially aligned, smooth, defect-free nanofibres with an average diameter of 160.2 ± 42.9 nm (Figure 2a). It is important to notice that the addition of the dispersions containing the nanomaterials did not compromise the stability/processability of the electrospinning solutions, just leading to a change of color to either brown (PG-GO and PG-GO_n) or black (PG-rGO and PG-rGO_n) without generating visible aggregates (Figure S4) nor requiring variations of the processing parameters. Nevertheless, the PG-GO nanofibrous system revealed distinctive morphological features such as micro-sized beads (Figure 2b) and GO sheets entangled with nanofibres (Figure 2c). The presence of these defects across the electrospun mesh is directly associated to a deficient encapsulating process of the bigger GO flakes into the polymer matrix.[42] Indeed, as it is shown in Figure 2d, the smaller size of the GO_n nanosheets originated a more suitable distribution and incorporation within the nanofibres and, consequently, a uniform and bead-free PG-GO_n network. Following this trend,

there was a larger number of exposed rGO flakes across the PG-rGO system (Figure 2e) comparatively to rGO_n nanosheets in respective PG-rGO_n electrospun nanofibres (Figure 2f).

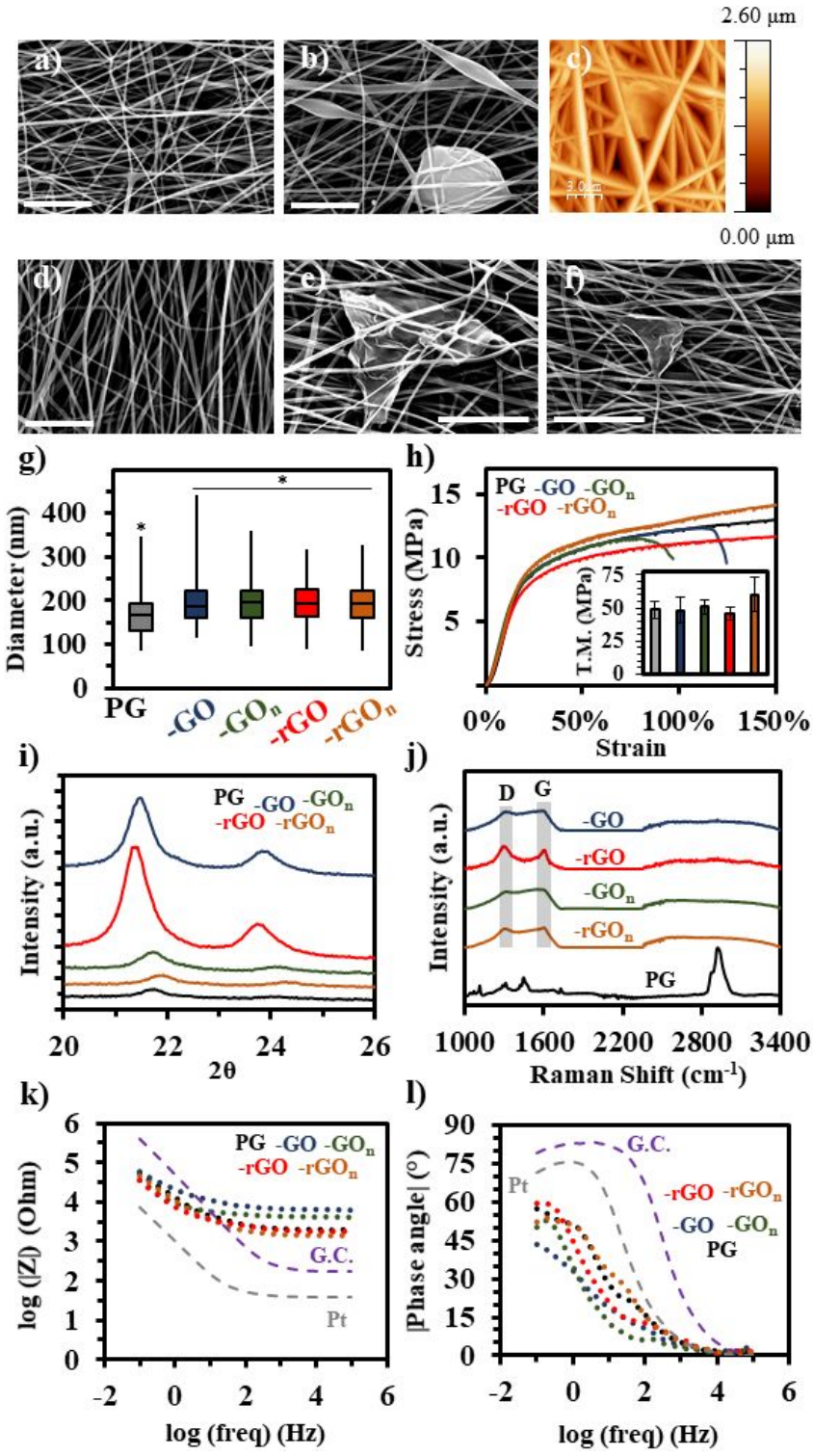

Figure 2. Characterization of electrospun nanofibres. Morphological analysis: **a)** PG; **b)** and **c)** PG-GO; **d)** PG-GO$_n$; **e)** PG-rGO; **f)** PG-rGO$_n$. Scale bars in SEM images = 5 µm. **g)** Nanofibres diameter box diagram. **h)** Mechanical analysis: stress-strain curves and tensile moduli (inset). **i)**

XRD spectra. **j)** Raman spectra. EIS measurements (Bode Plots): **k)** log(|impedance|) vs log(frequency) and **l)** |phase angle| vs log(frequency).

The diameter distributions of the nanofibres are summarized in Figure 2g, where the boxplot of each composition indicates the presence of a small portion of thin (< 150 nm) and thicker (> 250 nm) electrospun nanofibres, independently of the size and C/O ratios of the used nanomaterial. The average diameters of PG-GO (204.3 ± 70.3 nm), PG-GO_n (196.6 ± 45.8 nm), PG-rGO (201.9 ± 42.1 nm) and PG-rGO_n (193.2 ± 46.2 nm) samples proved to be higher comparatively to PG nanofibres, in accordance with other reported electrospun nanofibres presenting similar compositions.[43-44] Contrarily, work by Ramazani et al.[45] concluded that the incorporation of lower amounts of GO/rGO increases the conductivity of the electrospinning solution and, subsequently, diminishes the diameter of the composite electrospun nanofibres. Such discrepancies could be explained by differences involving the electrospinning parameters (e.g. voltage, concentration of the solution, solvent system, etc.).

The stress-strain curves of the electrospun networks (Figure 2h) indicate that the incorporation of both GO and GO_n provoked a decrease on the deformability and flexibility of the original PG nanofibres, leading to elongations at break of 115 ± 7.1 % and 80.7 ± 1.5 %, respectively. This is associated to a more restrictive movement of the polymer chains motivated by the interactions established between the oxygen containing groups located on the nanosheets and the PG matrix (e.g. hydrogen bonding). In the case of rGO and rGO_n, their higher C/O ratios enabled a stronger attachment to the PG polymer backbone via -CH2-π and/or van der Walls interactions.[45-47] Particularly, the superior mechanical reinforcement provided by rGO_n nanosheets induced a higher tensile modulus in PG-rGO_n nanofibres (60.0 ± 13.1 MPa), in comparison with values for PG (48.6 ± 6.3 MPa) and PG-GO_n (51.0 ± 5.5 MPa) electrospun

systems. There was no augmentation of the tensile modulus after incorporation of GO and rGO because of the interference of the large number of micro-beads and exposed sheets dispersed across PG-GO (48.4 ± 9.2 MPa) and PG-rGO (46.1 ± 4.8 MPa) nanofibrous networks. The alterations on the crystalline structure of PG nanofibres driven by the incorporation of the distinct nanomaterials are described in Figure 2i. Predictably, the XRD spectrum of the PG sample revealed the presence of a small peak (2θ = 21.72) associated to the crystallinity of PCL.[48] There was an additional peak also related to the PCL crystalline structure (2θ ~ 24) that slightly emerged in PG-GO_n and PG-rGO_n spectra and became clearly observable after the addition of GO and rGO (Table S1).[47] As a matter of fact, higher intensities of the XRD peaks occurred due to the ability of the nanosheets, especially the bigger ones, to act as nucleating agents on the PG matrix, boosting its crystallinity.[46-47, 49] Raman spectra of the electrospun systems (Figure 2j) confirmed a suitable dispersion/hybridization of all the nanomaterials onto the PG matrix. Specifically, their incorporation originated the appearance of the D and G bands characteristic of GO-related nanosheets, while the standard peaks of the crystalline fraction of PCL disappeared (Table S1).[22, 47] Relatively to the electrochemical properties, the impedance of each sample was measured in a wide range of frequencies and compared with very flat Pt and G.C. surfaces, as it is shown in Figure 2k. Briefly, although all the electrospun nanofibres proved to be inefficient conductors, it was the PG-GO network that presented the poorest conductive features, considering its higher |Z| values in all frequencies. A similar result was reported by González et al.,[50] who pointed out that, for both low and high frequencies, the presence of GO induced a non-significative decrease in the conductivity of the composite membrane relatively to the PCL control. In fact, for frequencies above ~ 1 Hz, the conductivity of each electrospun system was directly associated to the presence of sp^2 regions onto the incorporated nanomaterial

as higher C/O ratios provoked smaller |Z| values. There were no significant variations between the |Z| values of PG-rGO, PG-rGO_n and PG due to the considerable number of residual oxygen containing groups located onto the surfaces of the chemically reduced nanomaterials. The Phase angle data shown in Figure 2l is in accordance with the impedance results as it was possible to observe two different capacitive mechanisms in all samples. Both impedance and phase angle values presented a variability that could be related to small variations in exposed surface area to the electrolyte medium.

The capability of the electrospun meshes to support the growth of neural progenitor cells *in vitro* was evaluated by analyzing the morphology and viability of ENPCs after 14 days in culture. As observed by SEM (Figure 3), with the exception of PG-rGO_n, all the nanofibrous systems were able to support neural cell growth. The cells presented easily identifiable spherical somas and neurite extensions capable of outgrowing towards the electrospun nanofibres to guarantee intercellular connectivity. Opposite results were found on PG-rGO_n nanofibres, where spherical entities of smaller size, likely corresponding to apoptotic bodies, populated the matrix in the absence of evident neurites or even cell clusters characteristic of poorly adhesive substrates (Figure 3f). Comparatively to the PG-rGO electrospun network, where cells were able to efficaciously attach and use the exposed rGO flakes as focal adhesion points (Figure 3d and e), the presence of rGO_n nanosheets prevented an appropriate interaction between ENPCs and nanofibres (Figure 3g). Such discrepancy is probably associated to the impact of the dissimilar aggregation morphologies of rGO and rGO_n on protein adsorption, essential for maintaining enhanced cell-material interactions. Contrary to the gradual oxygen elimination that occurred from the edge to the center of the GO flakes, the lack of carboxylic groups onto the periphery of the GO_n nanosheets provoked an amplified “face-to-face” aggregation process during hydrazine

reduction.[36, 51] Hence, the resultant highly stacked rGO_n morphology presented a very limited available surface for adsorbing PLL and other proteins secreted by the cells. The fixation of PLL onto the surface of the nanofibres was probably a decisive factor, since it is a well-known protein able to enhance adhesion, growth and differentiation of ENPCs onto graphene substrates.[26, 30, 52] Comparatively, the presence of rGO sheets spread across the PCL-rGO electrospun network ensured a suitable PLL coating not only via electrostatic bonds generated by remaining oxygen functionalities, but also via hydrophobic and cation-π interactions.[53]

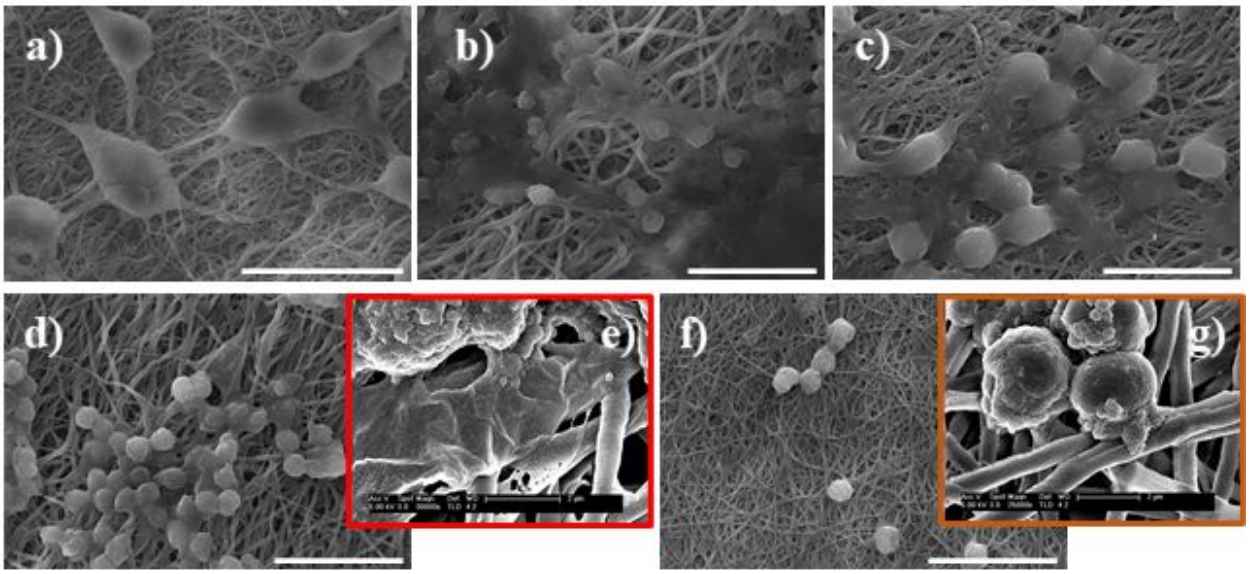

Figure 3. Representative SEM and fSEM images of ENPC cultures on electrospun nanofibres. **a)** PG; **b)** PG-GO; **c)** PG-GO_n; **d)** and **e)** PG-rGO; **f)** and **g)** PG-rGO_n. Scale bars in SEM images (a-d, f) = 20 μm. Scale bars in fSEM images (e, g) = 2 μm

These results were further confirmed by viability assays, as shown in Figure 4 and S5. As noticeable, PG, PG-GO, PG-GO_n and PG-rGO electrospun nanofibres were able to support highly viable cultures of homogeneously dispersed cells with typical neural morphology. Cell viability was significantly higher on PCL-rGO nanofibres relatively to PG-GO network, which is in agreement with the superior proficiency of the partially reduced state of GO to equilibrate

electrostatic, hydrophobic and hydrogen interactions with proteins in comparison to the highly oxygenated GO surfaces.[54-55] Complementarily, the dimensions and exposure of rGO sheets resulted on a far superior surface interface accessible for cell-material interactions, leading to a larger number of living cells comparatively to PG-GO_n. It is important to notice that, as expected, depending on the features of the incorporated nanomaterials, it was possible to camouflage the intrinsic bioactivity of PG and, consequently, modulate viability numbers (Figure 4g). Nonetheless, the incorporation of either GO or GO_n had no influence on cell viability relatively to original PG nanofibres. In any case, even when viability experienced no significant changes, differential effects on other cellular processes such as metabolic activity and neural function cannot be discarded. Further studies should be carried out to identify actions on other neural cell features induced by the presence of the distinct nanomaterials.

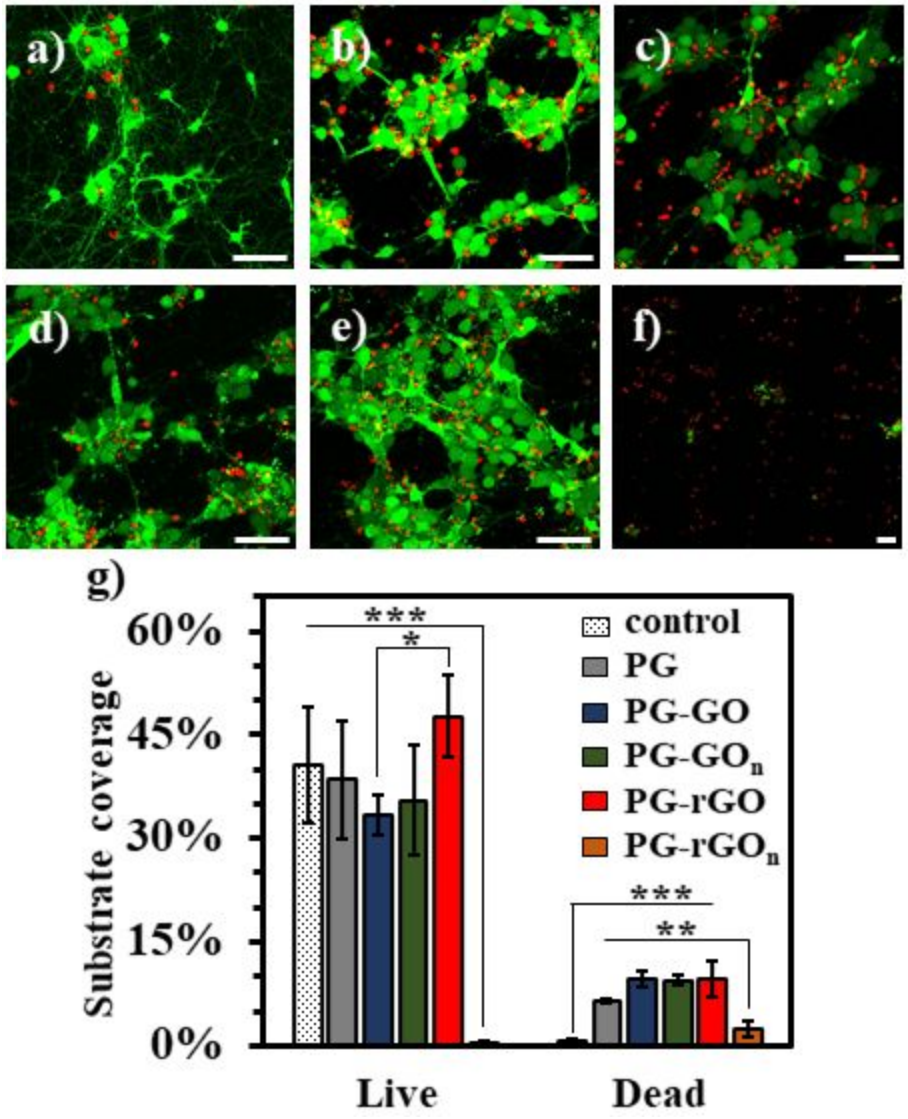

Figure 4. ENPCs viability studies on electrospun nanofibres. **a)** Control; **b)** PG; **c)** PG-GO; **d)** PG-GO$_n$; **e)** PG-rGO; **f)** PG-rGO$_n$. Scale bars = 50 μm. **g)** Quantification of ENPC viability on the different nanofibrous substrates.

Based on these results, both PG and PG-rGO electrospun meshes were selected as the best candidates to integrate the final fibrous-porous architecture of the 3D scaffolds.

3.3. 3D-PG and 3D-rGO scaffolds sustain highly viable and interconnected neural cultures

The concept behind the development of the 3D fibrous-porous architecture is that the synergetic combination of the biomimetic features of nanofibres and the bioactivity of graphene-based microporous structures could unlock a new scaffolding approach suitable to guarantee the formation and maintenance of highly viable neuronal networks. The microfabrication technique used to construct this scaffold was adapted from other reported methodologies, where dispersions of electrospun nanofibres were subjected to freeze-drying and crosslinking cycles to engineer 3D fibrous foams proficient for both *in vitro* and *in vivo* studies.[56-57] Herein, the small fragments of PG and PG-rGO electrospun meshes were simply dispersed into a rGO aqueous solution and vigorously mixed until hydrogel-like structures were formed. The hydrogels were generated in acidic medium (pH ~ 4) in order to induce a favorable network of attraction/repulsion forces between the negatively charged rGO (zeta potential = - 31 ± 0.6 mV) and the nanofibres. Indeed, similarly to other biopolymers (e.g. collagen), the gelatin content of the composite electrospun nanofibres could interact with the residual oxygen moieties of rGO sheets via electrostatic forces and hydrogen bonds.[58-59] Based on this hypothesis, the potential of the nanofibres to act as functional physical crosslinkers was evaluated via ATR-FTIR analysis. The 3D-PG spectrum (Figure 5a) comprised the characteristic peaks of its individual components, indicating the presence of alkoxy groups (C-O stretching at 1035 cm^{-1}), epoxy groups (asymmetric C-O-C stretching at 1245 cm^{-1}), hydroxyl groups (C-OH stretching at 1425 cm^{-1} and O-H stretching at 3100 – 3600 cm^{-1}) and carbonyl groups associated to the amide I vibration (at 1637 cm^{-1}) and the C=O stretching (at 1730 cm^{-1}).[47, 58] Similar functional groups were recognizable in the 3D-rGO ATR-FTIR spectrum (Figure 5b); yet, it was also possible to

identify an additional peak associated to the PG-rGO symmetric C-O-C stretching (1176 cm^{-1}). The occurrence of this particular peak revealed that the respective polymer chains in PG and PG-rGO were able to adopt different conformations/orientations when interfacing rGO sheets.[60] Nevertheless, the resultant 3D-PG and 3D-rGO scaffolds presented similar mechanisms for triggering the formation of fibrous-porous networks since the discernible shifting of their bands relative to their components was indicative of electrostatic interactions and hydrogen bonding.

After lyophilization, both 3D-PG (Figure 5c, d and S6) and 3D-rGO (Figure 5e, f and S7) scaffolds showed similar geometries composed of randomly interconnected micropores with irregular sizes and shapes as observed by SEM. As expected, distinctively from the typical graphene-based foams used for TE applications, the surface of the self-assembled rGO sheets were uniformly covered by electrospun nanofibres. In fact, nanofibres were exclusively attached onto rGO sheets, leading to a homogeneous 3D combinatorial network without notorious agglomerations of nanofibrous separated from the rGO system. Such successful coating could work as an additional biomimetic feature capable of boosting the inherent capacity of wrinkles and ripples of rGO surface to mimic neural ECM.[20, 61] Figure 5g compares the pore size distribution between 3D scaffolds, indicating that 3D-PG presented 61% of pores smaller than 100 μm, while the majority of pores (50%) composing 3D-rGO ranged from 100 to 200 μm. Such variations are intimately related to the superior capability of the PG nanofibres to mediate the repulsion forces between rGO sheets during the hydrogel formation, leading to a more pronounced contraction of the fibrous/porous network and, subsequently, to the formation of pores with smaller dimensions.[59]

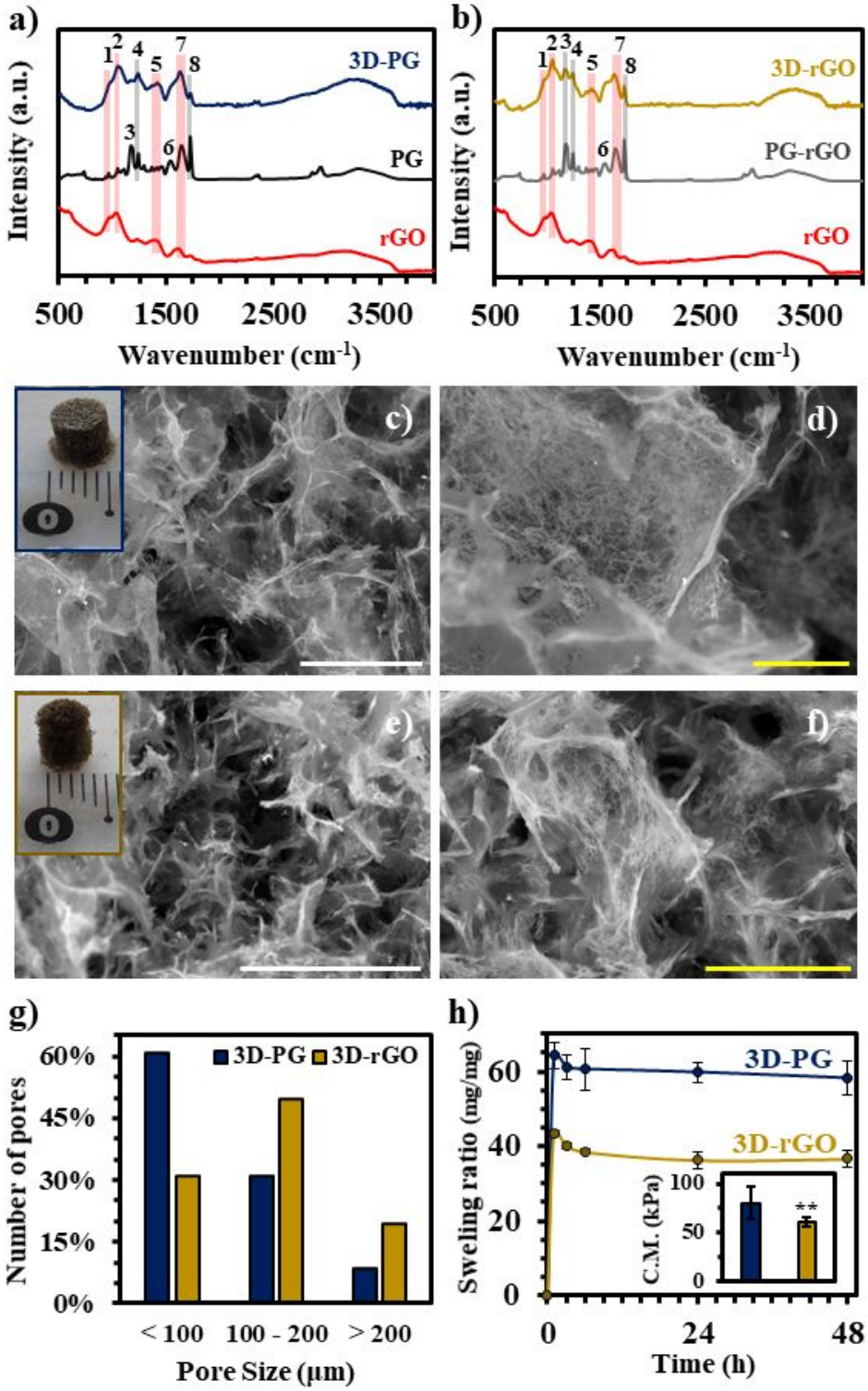

Figure 5. Characterization of 3D-PG and 3D-rGO scaffolds. ATR-FTIR spectra of the scaffolds: **a)** 3D-PG and **b)** 3D-rGO. Peaks: **1-** C-O-C; **2-** C-O; **3-** $_{s}$C-O-C; **4-** $_{A}$C-O-C; **5-** C-OH: **6-** Amide II; **7-** C=C and Amide I (C=O); and **8-** C=O. SEM analysis: **c)** and **d)** 3D-PG; **e)** and **f)** 3D-rGO.

Scale bars = 100 μm (white) and 40 μm (yellow). **g)** Pore size distribution of the scaffolds; **h)** Swelling properties and compressive moduli (inset) of the scaffolds.

Overall, although the 3D-rGO system had larger pores relatively to the 3D-PG, both scaffolds shown potential not only to promote cell infiltration, but also to ensure cell viability and communication via inwards transportation of nutrients and biochemical signals.[60, 62] It is noteworthy to mention that the presence of nanofibres was crucial to guarantee suitable porosities since the self-assembly of only rGO sheets resulted in a very compact structure (Figure S8a and b). Additionally, contrasting to 3D-PG and 3D-rGO scaffolds, the rGO construct was not able to maintain its structural integrity when immersed into water, disintegrating into heterogeneous clusters (Figure S8c). The water uptake capability of the scaffolds is summarized in Figure 5h, showing that the equilibrium was reached after 6 h at a swelling ratio of 60.6 ± 5.6 and 38.5 ± 0.6 for the 3D-PG and 3D-rGO, respectively. This result is related to both a barrier effect and the crosslinking induced by the rGO sheets dispersed in the PG-rGO electrospun system, which directly minimized the intake of water through this nanofibrous coating and therefore limited the swelling of the 3D-rGO scaffold.[63] Complementary, the rGO incorporation into the PG polymer matrix had compromised the proficiency of the PG-rGO nanofibres to mitigate the electrostatic repulsion forces between rGO sheets, leading to intermolecular interactions more exposed to disruptions provoked by water molecules.[59, 64] Therefore, as both electrostatic and hydrogen bonds were weakened during water uptake, the 3D-rGO fibrous-porous network was theoretically more exposed to a structural/mechanical decline relatively to the 3D-PG scaffold. However, there were no observable changes with respect to the original shapes of the scaffolds (Figure S9) or fragmentation of rGO/nanofibres evident into the water during the swelling process. The mechanical properties of the swollen scaffolds were in accordance to their distinct capacity to water uptake, resulting in a higher compressive modulus

for the 3D-PG (80.3 ± 8.9 kPa) comparatively to the 3D-rGO (60.9 ± 2.6 kPa). The compressive responses were studied until 20% of strain since above this value the scaffolds were unable to maintain a functional shape, becoming irrecoverably flattened. Their stress-strain curves are represented in Figure S9, where it was possible to identify linear and nonlinear regions for lower and higher strains, respectively. Considering that NSCs are capable of adapting their behavior with respect to the mechanical features of the substrate, scaffolds for neural TE are required to match the mechanical properties of either the brain (1-2 kPa), peripheral nerves (500 kPa - 8.1 MPa) or the spinal cord (40 kPa).[65-67] In this way, similarly to other reported graphene-based microporous systems, it is reasonable to envision future applications of these 3D-PG and 3D-rGO scaffolds for spinal cord TE strategies.[27, 54, 68]

Cell-material interactions established between the ENPCs and the scaffolds were evaluated after 14 days of culture, revealing that both 3D-PG and 3D-rGO were able to stimulate the formation of interconnected neural networks. Indeed, the combinatorial fibrous-porous architectures facilitated neural cell attachment and growth as confirmed by SEM (Figure 6 and S10). Furthermore, the topographic cues promoted complementary routes of intercellular communication, including close cell-cell interactions in areas with small pores (Figures 6a and d); cell bridging of larger micropores (until ~ 100 μm) to create intricate neuronal networks (Figures 6b and e); and the extension of long and robust cellular fascicules (nerve-like) to link distant sites with high cell densities (Figures 6c and f). The nanofibrous coating was more perceptible on guiding these neurites throughout the rGO sheets surface comparatively to areas where the ECM components were produced massively, covering the nanofibres. SEM images also confirmed that cells were allowed to migrate, eventually proliferate for those with such

ability, to interior regions of the scaffolds, particularly through micropores with dimensions larger than 50 μm (Figure S11).[60, 62]

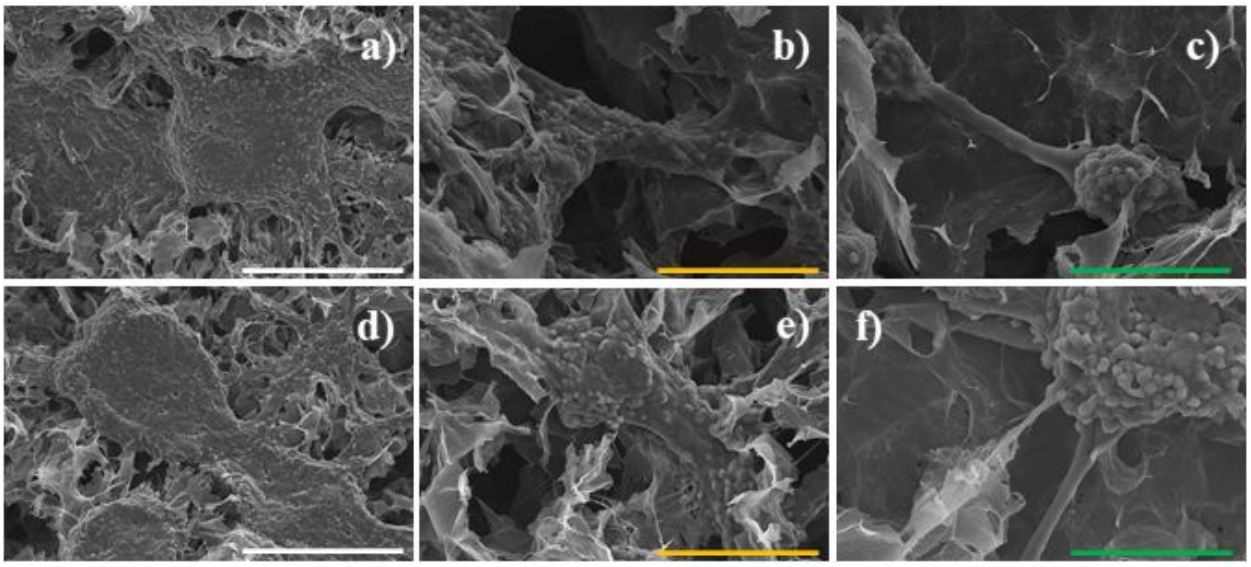

Figure 6. Representative SEM images of ENPC cultures on 3D scaffolds. **a-c)** 3D-PG; **d-f)** 3D-rGO. Scale bars = 200 μm (white), 100 μm (yellow) and 50 μm (green).

As illustrated in Figure 7, 3D-PG and 3D-rGO ensured the survival of the seeded ENPCs. The reduced number of dead cells was a compelling indicator of the stability of both samples *in vitro*, supporting the absence of a noticeable release of toxic degradation products driving toxicity issues. Viable cells were found to adapt their morphology and cell-cell connections to the topographical characteristics of the substrates either by surrounding the pores to cover all available surface, or by launching neurites below the surface to reach a nearby cell cluster (Figure S12). It is important to clarify that technical limitations have restricted the detection of cells to a colonization depth of approximately 200 μm (Figures are representative Z-stacks including ~ 100 planes of 2 μm of step-size each).

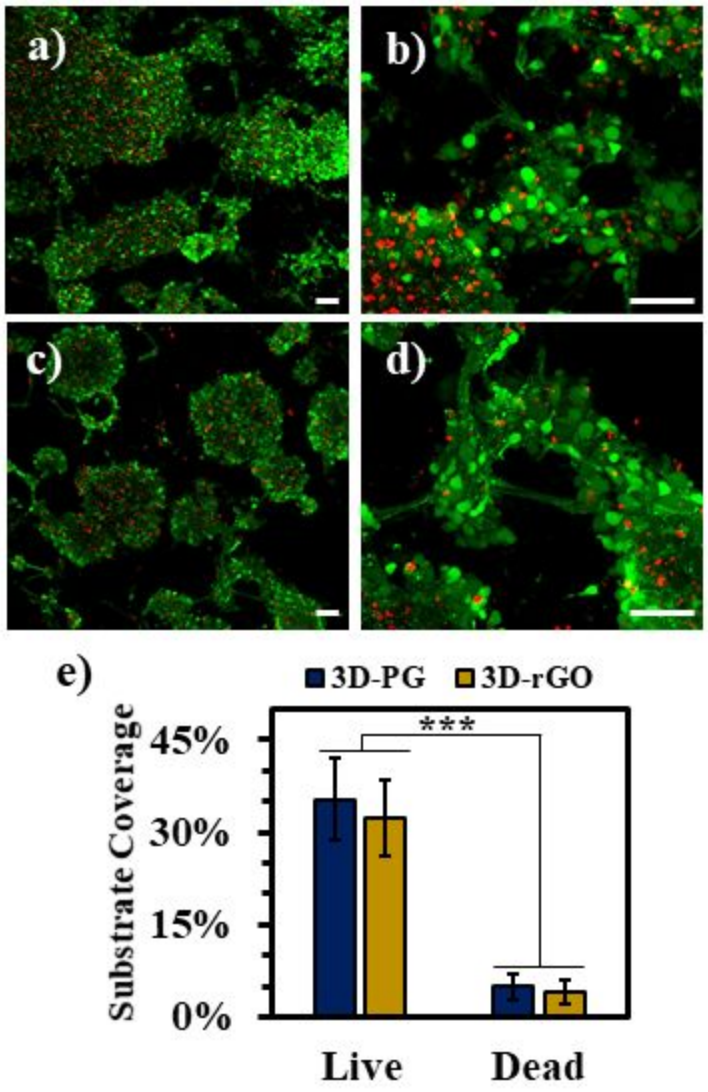

Figure 7. ENPC viability studies on 3D scaffolds. **a)** and **b)** 3D-PG; **c)** and **d)** 3D-rGO. Scale bars = 50 μm. **e)** Quantification of neural cell viability on the scaffolds.

Finally, the potential of 3D-PG and 3D-rGO scaffolds to induce the differentiation of the cultured ENPCs was evaluated by identifying specific markers of neuronal (map-2) and glial (vimentin) phenotypes. Figure 8 confirms the presence of both cell types in each scaffold, with a significant predominance of neurons, in accordance with other reported rGO-based substrates used for neural cell differentiation.[16, 26, 69] Generally, as it was described above, the small pores and random topographic irregularities (e.g. depressions) were preferential locations for the

accumulation of cell bodies.[24, 54] From these cell clusters occurred the elongation of neurites (marked with map-2), fasciculating in condensed bundles able to cover large areas with the purpose of connecting distant cells and generate more complex circuits (Figure S13). Although the differentiation patterns of NSCs could be successfully modulated by adapting the physicochemical characteristics of the graphene-based constructs (e.g. stiffness[25], reduction level[16], etc.), both 3D-PG and 3D-rGO presented similar percentages of neuronal and glial cell types, independently of their distinct mechanical/structural properties (Figure 8g). This result could be associated to the equivalent proportion of rGO used to recreate the two fibrous-porous systems. Indeed, comparatively to their nanofibrous components, the superior influence of the rGO sheets on facilitating PLL adsorption induced analogous ENPCs adhesion and neural branching in both scaffolds. Nonetheless, at 14 days of culture, the ability of 3D-PG and 3D-rGO to trigger an efficient neuronal differentiation influenced by the abundant presence of rGO was opposed by a slower differentiation and growth rate of glia-like cells. The described sequence of events corroborates the results from other reports, where PLL-coated rGO scaffolds started to present a residual number of glial cells that was progressively increasing and even surpassed the neuronal population after longer culture periods (21 days), as expected from the culture conditions used herein.[26, 54]

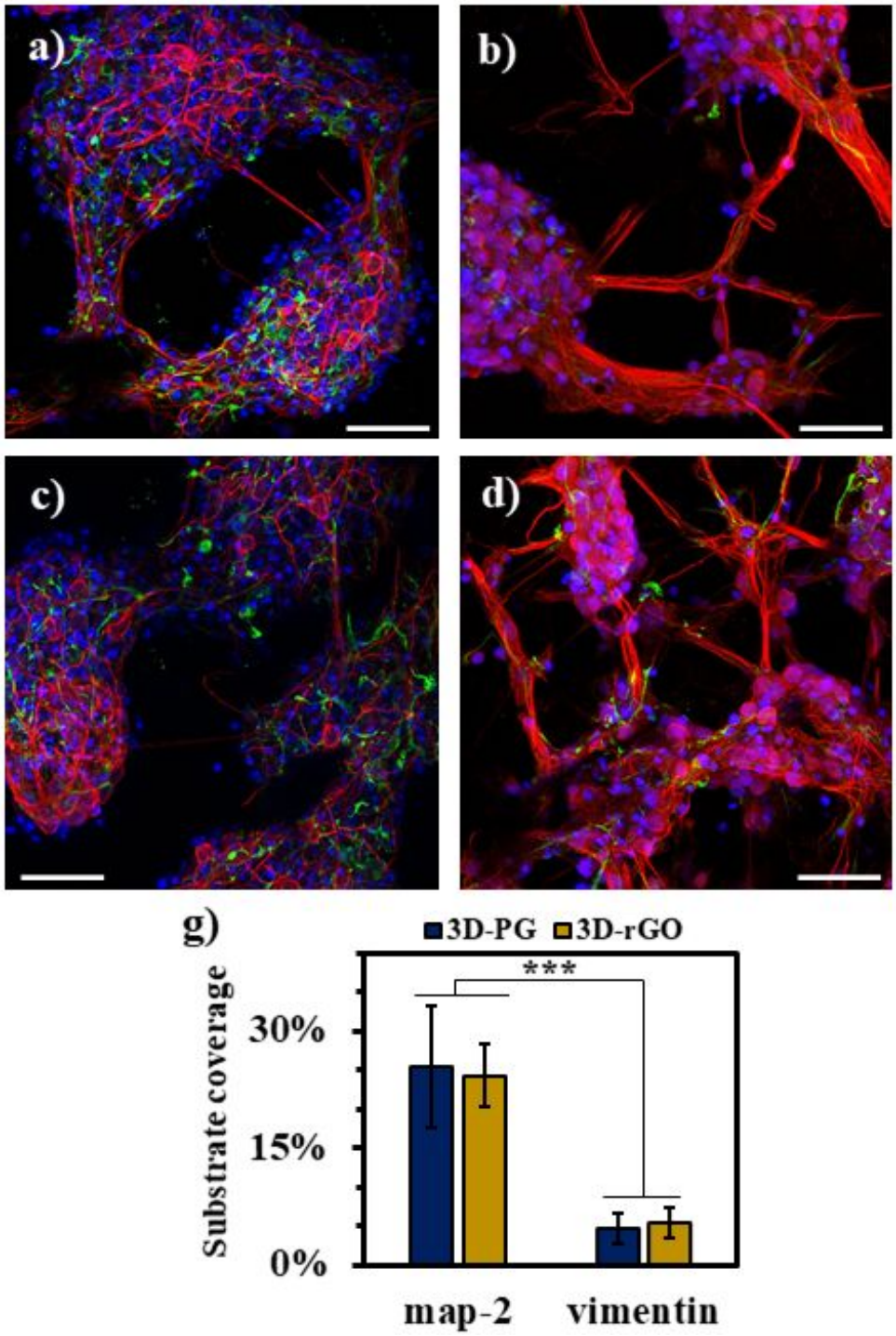

Figure 8. ENPCs differentiation studies on 3D scaffolds. **a)** and **b)** 3D-PG; **c)** and **d)** 3D-rGO. Map-2 (red); vimentin (green) and cell nuclei (blue). Scale bars = 50 μm. **e)** Quantification of neural cell differentiation on the scaffolds.

In summary, both 3D-PG and 3D-rGO scaffolds proved to support the generation of highly viable neural networks *in vitro*. These promising results relied on an original scaffolding approach capable of successfully engineering 3D fibrous-porous architectures, where the physicochemical features of rGO sheets were synergistically combined with biomimetic coatings of PG electrospun nanofibres. Indeed, as the nanofibres covered the surface of the rGO sheets, it was possible to safeguard an optimized outgrowth and guidance of neural bundles, leading to the connection of distant sites of the scaffold with the purpose of forming complex circuits. Pivotal neural cell responses such as adhesion, branching and differentiation were primarily influenced by the favorable features of the rGO sheets, which were enhanced after an efficient adsorption of PLL. The accommodation, distribution and infiltration of cells in the developed 3D scaffolds were stimulated by their heterogeneous microporous systems. In fact, the structural/mechanical integrities as well as pore size distributions of the scaffolds were adjusted by each specific network of attraction/repulsion forces established during the 3D-PG and 3D-rGO hydrogels synthesis. This particular result could be crucial for upcoming *in vivo* studies, in which 3D fibrous-porous scaffolds must accommodate specific characteristics of the targeted neural cell microenvironment, including mechanical compliance, swelling ability and porosity. Overall, these findings validate a feasible and customizable methodology to construct neural TE scaffolds and encourage future *in vivo* investigations, particularly aiming injured spinal cord regeneration.

4. Conclusion

We report a new scaffolding methodology proficient to upgrade standard rGO microporous networks by the incorporation of biomimetic coatings of electrospun nanofibres. The final 3D fibrous-porous systems, which properties were customized accordingly to the specific features of their nanofibrous components, were capable of enhancing the differentiation of ENPCs to both

neurons and glial cells, supporting the formation of viable and interconnected neural circuits *in vitro*. Overall, these scaffolds show promise as novel 3D platforms for neural TE applications.

ASSOCIATED CONTENT

Supporting Information: Nanomaterials: additional AFM and XPS information. Nanofibres: electrospinning solutions image; structural characterization (XRD and Raman); additional ENPC viability images. 3D scaffolds: additional SEM images; control studies; compressive stress-strain curves; additional ENPCs images regarding morphology, viability and differentiation studies.

AUTHOR INFORMATION

Corresponding Authors

*MCS: mc.terradas@csic.es ; *PAAPM: paulam@ua.pt

Author Contributions

AFG: Conceptualization; Investigation (fabrication and characterization of all materials/substrates, cell culture); Writing – original draft. **JS:** Investigation (fabrication and characterization of the nanomaterials/nanofibres). **ADB** and **AGM**: Investigation (cell culture). **IB**: Investigation (AFM analysis). **EPO** and **NCP**: Investigation (design and measurements of EIS studies). **MJH** and **GOI**: Investigation (XPS analysis). **AC**: Supervision; Writing – review & editing. **MCS** and **PAAPM**: Conceptualization; Supervision; Writing – review & editing.

All authors have given approval to the final version of the manuscript.

ACKNOWLEDGMENT

This work was supported by the projects UIDB/00481/2020 and UIDP/00481/2020 - FCT - Fundação para a Ciência e a Tecnologia; and CENTRO-01-0145-FEDER-022083 - Centro Portugal Regional Operational Programme (Centro2020), under the PORTUGAL 2020 Partnership Agreement, through the European Regional Development Fund; and *Agencia Estatal de Investigación of Spain and the Fondo Europeo de Desarrollo Regional* (MAT2016-78857-R, AEI/FEDER, UE); RTI2018-097753-B-I00, and Severo Ochoa Program (SEV-2015-0496). AFG thanks to FCT for the PhD grant SFRH/BD/130287/2017, which is carried out in collaboration between TEMA-UA and ICMM-CSIC. JS thanks to FCT for the PhD grant SFRH/BD/144579/2019. IB thanks to FCT for the financial support (IF/00582/2015).

REFERENCES

(1) Kumar, S.; Chatterjee, K. Comprehensive Review on the Use of Graphene-Based Substrates for Regenerative Medicine and Biomedical Devices. *ACS Appl. Mater. Interfaces* **2016,** *8*, 26431-26457.

(2) Kostarelos, K.; Vincent, M.; Hebert, C.; Garrido, J. A. Graphene in the Design and Engineering of Next-Generation Neural Interfaces. *Adv. Mater.* **2017,** *29*, 1700909.

(3) Bramini, M.; Alberini, G.; Colombo, E.; Chiacchiaretta, M.; DiFrancesco, M. L.; Maya-Vetencourt, J. F.; Maragliano, L.; Benfenati, F.; Cesca, F. Interfacing Graphene-Based Materials With Neural Cells. *Front. Syst. Neurosci.* **2018,** *12*.

(4) Akhavan, O. Graphene scaffolds in progressive nanotechnology/stem cell-based tissue engineering of the nervous system. *J Mater Chem B* **2016,** *4*, 3169-3190.

(5) Dreyer, D. R.; Park, S.; Bielawski, C. W.; Ruoff, R. S. The chemistry of graphene oxide. *Chem. Soc. Rev.* **2010,** *39*, 228-240.

(6) Rauti, R.; Lozano, N.; León, V.; Scaini, D.; Musto, M.; Rago, I.; Ulloa Severino, F. P.; Fabbro, A.; Casalis, L.; Vázquez, E.; Kostarelos, K.; Prato, M.; Ballerini, L. Graphene Oxide Nanosheets Reshape Synaptic Function in Cultured Brain Networks. *ACS Nano* **2016,** *10*, 4459-4471.

(7) Chiacchiaretta, M.; Bramini, M.; Rocchi, A.; Armirotti, A.; Giordano, E.; Vázquez, E.; Bandiera, T.; Ferroni, S.; Cesca, F.; Benfenati, F. Graphene Oxide Upregulates the Homeostatic Functions of Primary Astrocytes and Modulates Astrocyte-to-Neuron Communication. *Nano Lett.* **2018,** *18*, 5827-5838.

(8) Bramini, M.; Sacchetti, S.; Armirotti, A.; Rocchi, A.; Vázquez, E.; León Castellanos, V.; Bandiera, T.; Cesca, F.; Benfenati, F. Graphene Oxide Nanosheets Disrupt Lipid Composition, Ca2+ Homeostasis, and Synaptic Transmission in Primary Cortical Neurons. *ACS Nano* **2016,** *10*, 7154-7171.

(9) Rauti, R.; Medelin, M.; Newman, L.; Vranic, S.; Reina, G.; Bianco, A.; Prato, M.; Kostarelos, K.; Ballerini, L. Graphene Oxide Flakes Tune Excitatory Neurotransmission in Vivo by Targeting Hippocampal Synapses. *Nano Lett.* **2019,** *19*, 2858-2870.

(10) Tu, Q.; Pang, L.; Chen, Y.; Zhang, Y.; Zhang, R.; Lu, B.; Wang, J. Effects of surface charges of graphene oxide on neuronal outgrowth and branching. *Analyst* **2014,** *139*, 105-115.

(11) Durso, M.; Borrachero-Conejo, A. I.; Bettini, C.; Treossi, E.; Scidà, A.; Saracino, E.; Gazzano, M.; Christian, M.; Morandi, V.; Tuci, G.; Giambastiani, G.; Ottaviano, L.; Perrozzi, F.;

Benfenati, V.; Melucci, M.; Palermo, V. Biomimetic graphene for enhanced interaction with the external membrane of astrocytes. *J Mater Chem B* **2018,** *6*, 5335-5342.

(12) Weaver, C. L.; Cui, X. T. Directed Neural Stem Cell Differentiation with a Functionalized Graphene Oxide Nanocomposite. *Adv. Healthc. Mater.* **2015,** *4*, 1408-1416.

(13) Yang, K.; Lee, J.; Lee, J. S.; Kim, D.; Chang, G.-E.; Seo, J.; Cheong, E.; Lee, T.; Cho, S.-W. Graphene Oxide Hierarchical Patterns for the Derivation of Electrophysiologically Functional Neuron-like Cells from Human Neural Stem Cells. *ACS Appl. Mater. Interfaces* **2016,** *8*, 17763-17774.

(14) Pei, S.; Cheng, H.-M. The reduction of graphene oxide. *Carbon* **2012,** *50*, 3210-3228.

(15) Sydlik, S. A.; Jhunjhunwala, S.; Webber, M. J.; Anderson, D. G.; Langer, R. In Vivo Compatibility of Graphene Oxide with Differing Oxidation States. *ACS Nano* **2015,** *9*, 3866-3874.

(16) Akhavan, O.; Ghaderi, E.; Abouei, E.; Hatamie, S.; Ghasemi, E. Accelerated differentiation of neural stem cells into neurons on ginseng-reduced graphene oxide sheets. *Carbon* **2014,** *66*, 395-406.

(17) Heidari, M.; Bahrami, S. H.; Ranjbar-Mohammadi, M.; Milan, P. B. Smart electrospun nanofibers containing PCL/gelatin/graphene oxide for application in nerve tissue engineering. *Mater. Sci. Eng. C* **2019,** *103*, 109768.

(18) Wang, J.; Cheng, Y.; Chen, L.; Zhu, T.; Ye, K.; Jia, C.; Wang, H.; Zhu, M.; Fan, C.; Mo, X. In vitro and in vivo studies of electroactive reduced graphene oxide-modified nanofiber scaffolds for peripheral nerve regeneration. *Acta Biomater.* **2019,** *84*, 98-113.

(19) Shah, S.; Yin, P. T.; Uehara, T. M.; Chueng, S.-T. D.; Yang, L.; Lee, K.-B. Guiding Stem Cell Differentiation into Oligodendrocytes Using Graphene-Nanofiber Hybrid Scaffolds. *Adv. Mater.* **2014,** *26*, 3673-3680.

(20) Zhang, K.; Zheng, H.; Liang, S.; Gao, C. Aligned PLLA nanofibrous scaffolds coated with graphene oxide for promoting neural cell growth. *Acta Biomater.* **2016,** *37*, 131-142.

(21) Wang, L.; Liu, X.; Fu, J.; Ning, X.; Zhang, M.; Jiang, Z.; Cheng, G.; Zhu, Y.; Zhang, Z. Release of methylene blue from graphene oxide-coated electrospun nanofibrous scaffolds to modulate functions of neural progenitor cells. *Acta Biomater.* **2019,** *88*, 346-356.

(22) Song, J.; Gao, H.; Zhu, G.; Cao, X.; Shi, X.; Wang, Y. The preparation and characterization of polycaprolactone/graphene oxide biocomposite nanofiber scaffolds and their application for directing cell behaviors. *Carbon* **2015,** *95*, 1039-1050.

(23) Qing, H.; Jin, G.; Zhao, G.; Huang, G.; Ma, Y.; Zhang, X.; Sha, B.; Luo, Z.; Lu, T. J.; Xu, F. Heterostructured Silk-Nanofiber-Reduced Graphene Oxide Composite Scaffold for SH-SY5Y Cell Alignment and Differentiation. *ACS Appl. Mater. Interfaces* **2018,** *10*, 39228-39237.

(24) Akhavan, O.; Ghaderi, E.; Shirazian, S. A.; Rahighi, R. Rolled graphene oxide foams as three-dimensional scaffolds for growth of neural fibers using electrical stimulation of stem cells. *Carbon* **2016,** *97*, 71-77.

(25) Ma, Q.; Yang, L.; Jiang, Z.; Song, Q.; Xiao, M.; Zhang, D.; Ma, X.; Wen, T.; Cheng, G. Three-Dimensional Stiff Graphene Scaffold on Neural Stem Cells Behavior. *ACS Appl. Mater. Interfaces* **2016,** *8*, 34227-34233.

(26) Serrano, M. C.; Patiño, J.; García-Rama, C.; Ferrer, M. L.; Fierro, J. L. G.; Tamayo, A.; Collazos-Castro, J. E.; del Monte, F.; Gutiérrez, M. C. 3D free-standing porous scaffolds made of graphene oxide as substrates for neural cell growth. *J Mater Chem B* **2014,** *2*, 5698-5706.

(27) Domínguez-Bajo, A.; González-Mayorga, A.; Guerrero, C. R.; Palomares, F. J.; García, R.; López-Dolado, E.; Serrano, M. C. Myelinated axons and functional blood vessels populate mechanically compliant rGO foams in chronic cervical hemisected rats. *Biomaterials* **2019,** *192*, 461-474.

(28) Gonçalves, G.; Vila, M.; Bdikin, I.; de Andrés, A.; Emami, N.; Ferreira, R. A. S.; Carlos, L. D.; Grácio, J.; Marques, P. A. A. P. Breakdown into nanoscale of graphene oxide: Confined hot spot atomic reduction and fragmentation. *Sci. Rep.* **2014,** *4*, 6735.

(29) Carballo-Vila, M.; Moreno-Burriel, B.; Chinarro, E.; Jurado, J. R.; Casan-Pastor, N.; Collazos-Castro, J. E. Titanium oxide as substrate for neural cell growth. *J Biomed Mater Res A* **2009,** *90*, 94-105.

(30) Serrano, M. C.; Feito, M. J.; González-Mayorga, A.; Diez-Orejas, R.; Matesanz, M. C.; Portolés, M. T. Response of macrophages and neural cells in contact with reduced graphene oxide microfibers. *Biomaterials Science* **2018,** *6*, 2987-2997.

(31) Coleman, B. R.; Knight, T.; Gies, V.; Jakubek, Z. J.; Zou, S. Manipulation and Quantification of Graphene Oxide Flake Size: Photoluminescence and Cytotoxicity. *ACS Appl. Mater. Interfaces* **2017,** *9*, 28911-28921.

(32) Ren, P.-G.; Yan, D.-X.; Ji, X.; Chen, T.; Li, Z.-M. Temperature dependence of graphene oxide reduced by hydrazine hydrate. *Nanotechnology* **2010,** *22*, 055705.

(33) Gholampour, A.; Valizadeh Kiamahalleh, M.; Tran, D. N. H.; Ozbakkaloglu, T.; Losic, D. From Graphene Oxide to Reduced Graphene Oxide: Impact on the Physiochemical and Mechanical Properties of Graphene–Cement Composites. *ACS Appl. Mater. Interfaces* **2017,** *9*, 43275-43286.

(34) Gao, X.; Jang, J.; Nagase, S. Hydrazine and Thermal Reduction of Graphene Oxide: Reaction Mechanisms, Product Structures, and Reaction Design. *J. Phys. Chem. C* **2010,** *114*, 832-842.

(35) Huang, H.-H.; De Silva, K. K. H.; Kumara, G. R. A.; Yoshimura, M. Structural Evolution of Hydrothermally Derived Reduced Graphene Oxide. *Sci. Rep.* **2018,** *8*, 6849.

(36) Su, H.; Zhang, C.; Li, X.; Wu, L.; Chen, Y. Aggregation prevention: reduction of graphene oxide in mixed medium of alkylphenol polyoxyethylene (7) ether and 2-methoxyethanol. *RSC Adv.* **2018,** *8*, 39140-39148.

(37) Krishnamoorthy, K.; Veerapandian, M.; Yun, K.; Kim, S. J. The chemical and structural analysis of graphene oxide with different degrees of oxidation. *Carbon* **2013,** *53*, 38-49.

(38) Li, M.-j.; Liu, C.-m.; Xie, Y.-b.; Cao, H.-b.; Zhao, H.; Zhang, Y. The evolution of surface charge on graphene oxide during the reduction and its application in electroanalysis. *Carbon* **2014,** *66*, 302-311.

(39) Park, S.; An, J.; Potts, J. R.; Velamakanni, A.; Murali, S.; Ruoff, R. S. Hydrazine-reduction of graphite- and graphene oxide. *Carbon* **2011,** *49*, 3019-3023.

(40) Wu, J.-B.; Lin, M.-L.; Cong, X.; Liu, H.-N.; Tan, P.-H. Raman spectroscopy of graphene-based materials and its applications in related devices. *Chem. Soc. Rev.* **2018,** *47*, 1822-1873.

(41) Shen, L.; Zhang, L.; Wang, K.; Miao, L.; Lan, Q.; Jiang, K.; Lu, H.; Li, M.; Li, Y.; Shen, B.; Zheng, W. Analysis of oxidation degree of graphite oxide and chemical structure of corresponding reduced graphite oxide by selecting different-sized original graphite. *RSC Adv.* **2018,** *8*, 17209-17217.

(42) Jalaja, K.; Sreehari, V. S.; Kumar, P. R. A.; Nirmala, R. J. Graphene oxide decorated electrospun gelatin nanofibers: Fabrication, properties and applications. *Mater. Sci. Eng. C* **2016,** *64*, 11-19.

(43) Chen, X.; Feng, B.; Zhu, D.-Q.; Chen, Y.-W.; Ji, W.; Ji, T.-J.; Li, F. Characteristics and toxicity assessment of electrospun gelatin/PCL nanofibrous scaffold loaded with graphene in vitro and in vivo. *Int J Nanomedicine* **2019,** *14*, 3669-3678.

(44) Wan, C.; Chen, B. Poly(ε-caprolactone)/graphene oxide biocomposites: mechanical properties and bioactivity. *Biomed. Mater.* **2011,** *6*, 055010.

(45) Ramazani, S.; Karimi, M. Aligned poly(ε-caprolactone)/graphene oxide and reduced graphene oxide nanocomposite nanofibers: Morphological, mechanical and structural properties. *Mater. Sci. Eng. C* **2015,** *56*, 325-334.

(46) Heidari, M.; Bahrami, H.; Ranjbar-Mohammadi, M. Fabrication, optimization and characterization of electrospun poly(caprolactone)/gelatin/graphene nanofibrous mats. *Mater. Sci. Eng. C* **2017,** *78*, 218-229.

(47) Ramazani, S.; Karimi, M. Study the molecular structure of poly(ε-caprolactone)/graphene oxide and graphene nanocomposite nanofibers. *J Mech Behav Biomed* **2016,** *61*, 484-492.

(48) Gautam, S.; Dinda, A. K.; Mishra, N. C. Fabrication and characterization of PCL/gelatin composite nanofibrous scaffold for tissue engineering applications by electrospinning method. *Mater. Sci. Eng. C* **2013,** *33*, 1228-1235.

(49) Wang, B.; Li, Y.; Weng, G.; Jiang, Z.; Chen, P.; Wang, Z.; Gu, Q. Reduced graphene oxide enhances the crystallization and orientation of poly(ε-caprolactone). *Compos. Sci. Technol.* **2014,** *96*, 63-70.

(50) Sánchez-González, S.; Diban, N.; Bianchi, F.; Ye, H.; Urtiaga, A. Evidences of the Effect of GO and rGO in PCL Membranes on the Differentiation and Maturation of Human Neural Progenitor Cells. *Macromol. Biosci.* **2018,** *18*, 1800195.

(51) Qi, Y.; Chen, W.; Liu, F.; Liu, J.; Zhang, T.; Chen, W. Aggregation morphology is a key factor determining protein adsorption on graphene oxide and reduced graphene oxide nanomaterials. *Environ. Sci. Nano* **2019,** *6*, 1303-1309.

(52) González-Mayorga, A.; López-Dolado, E.; Gutiérrez, M. C.; Collazos-Castro, J. E.; Ferrer, M. L.; del Monte, F.; Serrano, M. C. Favorable Biological Responses of Neural Cells and Tissue Interacting with Graphene Oxide Microfibers. *ACS Omega* **2017,** *2*, 8253-8263.

(53) Wang, J.; Zhao, Y.; Ma, F.-X.; Wang, K.; Wang, F.-B.; Xia, X.-H. Synthesis of a hydrophilic poly-l-lysine/graphene hybrid through multiple non-covalent interactions for biosensors. *J Mater Chem B* **2013,** *1*, 1406-1413.

(54) Shi, X.; Chang, H.; Chen, S.; Lai, C.; Khademhosseini, A.; Wu, H. Regulating Cellular Behavior on Few-Layer Reduced Graphene Oxide Films with Well-Controlled Reduction States. *Adv. Funct. Mater.* **2012,** *22*, 751-759.

(55) Kumar, S.; Parekh, S. H. Linking graphene-based material physicochemical properties with molecular adsorption, structure and cell fate. *Commun. Chem.* **2020,** *3*, 8.

(56) Miszuk, J. M.; Xu, T.; Yao, Q.; Fang, F.; Childs, J. D.; Hong, Z.; Tao, J.; Fong, H.; Sun, H. Functionalization of PCL-3D electrospun nanofibrous scaffolds for improved BMP2-induced bone formation. *Appl. Mater. Today* **2018,** *10*, 194-202.

(57) Sun, B.; Zhou, Z.; Wu, T.; Chen, W.; Li, D.; Zheng, H.; El-Hamshary, H.; Al-Deyab, S. S.; Mo, X.; Yu, Y. Development of Nanofiber Sponges-Containing Nerve Guidance Conduit for Peripheral Nerve Regeneration in Vivo. *ACS Appl. Mater. Interfaces* **2017,** *9*, 26684-26696.

(58) Piao, Y.; Chen, B. Self-assembled graphene oxide–gelatin nanocomposite hydrogels: Characterization, formation mechanisms, and pH-sensitive drug release behavior. *J Polym Sci B Polym Phys* **2015,** *53*, 356-367.

(59) Girão, A. F.; Gonçalves, G.; Bhangra, K. S.; Phillips, J. B.; Knowles, J.; Irurueta, G.; Singh, M. K.; Bdkin, I.; Completo, A.; Marques, P. A. A. P. Electrostatic self-assembled graphene oxide-collagen scaffolds towards a three-dimensional microenvironment for biomimetic applications. *RSC Adv.* **2016,** *6*, 49039-49051.

(60) Elzein, T.; Nasser-Eddine, M.; Delaite, C.; Bistac, S.; Dumas, P. FTIR study of polycaprolactone chain organization at interfaces. *J. Colloid Interface Sci.* **2004,** *273*, 381-387.

(61) Ma, X.; Xiao, M.; Hao, Y.; Cheng, G. Precisely controllable hybrid graphene scaffold reveals size effects on differentiation of neural progenitor cells in mimicking neural network. *Carbon* **2019,** *145*, 90-99.

(62) Guo, W.; Wang, S.; Yu, X.; Qiu, J.; Li, J.; Tang, W.; Li, Z.; Mou, X.; Liu, H.; Wang, Z. Construction of a 3D rGO–collagen hybrid scaffold for enhancement of the neural differentiation of mesenchymal stem cells. *Nanoscale* **2016,** *8*, 1897-1904.

(63) Panzavolta, S.; Bracci, B.; Gualandi, C.; Focarete, M. L.; Treossi, E.; Kouroupis-Agalou, K.; Rubini, K.; Bosia, F.; Brely, L.; Pugno, N. M.; Palermo, V.; Bigi, A. Structural reinforcement and failure analysis in composite nanofibers of graphene oxide and gelatin. *Carbon* **2014,** *78*, 566-577.

(64) Huang, Y.; Zeng, M.; Feng, Z.; Yin, D.; Xu, Q.; Fan, L. Graphene oxide-based composite hydrogels with self-assembled macroporous structures. *RSC Adv.* **2016,** *6*, 3561-3570.

(65) Fan, L.; Liu, C.; Chen, X.; Zou, Y.; Zhou, Z.; Lin, C.; Tan, G.; Zhou, L.; Ning, C.; Wang, Q. Directing Induced Pluripotent Stem Cell Derived Neural Stem Cell Fate with a Three-Dimensional Biomimetic Hydrogel for Spinal Cord Injury Repair. *ACS Appl. Mater. Interfaces* **2018,** *10*, 17742-17755.

(66) Alegret, N.; Dominguez-Alfaro, A.; González-Domínguez, J. M.; Arnaiz, B.; Cossío, U.; Bosi, S.; Vázquez, E.; Ramos-Cabrer, P.; Mecerreyes, D.; Prato, M. Three-Dimensional Conductive Scaffolds as Neural Prostheses Based on Carbon Nanotubes and Polypyrrole. *ACS Appl. Mater. Interfaces* **2018,** *10*, 43904-43914.

(67) Ryan, A. J.; Lackington, W. A.; Hibbitts, A. J.; Matheson, A.; Alekseeva, T.; Stejskalova, A.; Roche, P.; O'Brien, F. J. A Physicochemically Optimized and Neuroconductive Biphasic Nerve Guidance Conduit for Peripheral Nerve Repair. *Adv. Healthc. Mater.* **2017,** *6*, 1700954.

(68) López-Dolado, E.; González-Mayorga, A.; Gutiérrez, M. C.; Serrano, M. C. Immunomodulatory and angiogenic responses induced by graphene oxide scaffolds in chronic spinal hemisected rats. *Biomaterials* **2016,** *99*, 72-81.

(69) Guo, W.; Qiu, J.; Liu, J.; Liu, H. Graphene microfiber as a scaffold for regulation of neural stem cells differentiation. *Sci. Rep.* **2017,** *7*, 5678.

GRAPHICAL ABSTRACT: